Sensors and Materials, Vol. 38, No. 3 (2026) 1283–1302
MYU Tokyo

S & M 4377

Tripping-induced Fall Detection Using Dual-torso Inertial Measurement Units: An Experimental Evaluation with Long Short-term Memory

Jin Zhang,[1*] Takuya Tajima,[2] and Takehiko Abe[3]

[1]Intelligent Information System Engineering, Fukuoka Institute of Technology, 3-30-1 Wajiro-higashi, Higashi-ku, Fukuoka 811-0295 Japan
[2]Intelligent Information System Engineering, Fukuoka Institute of Technology, 3-30-1 Wajiro-higashi, Higashi-ku, Fukuoka 811-0295 Japan
[3]Department of Economics, Aichi University, 4-60-6 Hiraike-cho, Nakamura-ku, Nagoya Aichi 453-8777 Japan

(Received November 25, 2025; accepted February 13, 2026)

Keywords: tripping-induced fall detection, long short-term memory, dual inertial measurement units

With the growing aging population, the demand for reliable fall detection systems is increasing. Owing to safety concerns, real-world fall data—especially for tripping-induced falls—are often limited in existing studies. To address this limitation, we developed a large-scale fall-protection system and conducted controlled experiments specifically targeting tripping falls, ensuring subject safety throughout. Subjects wore two inertial measurement units mounted on the torso—one on the chest and the other on the abdomen—and performed both tripping falls and fall-like behaviors. These wearable inertial sensors continuously captured torso motion signals, providing time-series acceleration and angular velocity data for subsequent analysis. On the basis of the collected time-series data, three long short-term memory-based models were developed: two single-sensor models and one dual-sensor model. A leave-one-subject-out cross-validation approach was applied, and a low sigmoid decision threshold together with a consecutive-window decision rule was adopted to reduce missed detections. Experimental results demonstrated high classification performance across all models, with the dual-sensor model achieving the best accuracy, precision, recall, and F1-score. These findings confirm the effectiveness of the proposed method in distinguishing tripping falls from similar daily activities.

1. Introduction

According to statistics from the Tokyo Fire Department, approximately 80% of accidents involving the elderly are caused by falls, and in 2021 alone, 53675 elderly people were transported to hospitals in an emergency due to falls.(1) According to an announcement by the Japanese Ministry of Health, Labor and Welfare (2022),(2) the number of people waiting for admission to special nursing homes for the elderly is 253000. Although there has been a

*Corresponding author: e-mail: jinzhang442@gmail.com
https://doi.org/10.18494/SAM6078

ISSN 0914-4935
https://myukk.org/

downward trend since 2014, there are still many people waiting. However, many nursing homes are not accepting people owing to difficulties in dealing with medical care and dementia.[3]

In our previous research,[4,5] we tried to classify the attribute of whether a walker is prone to fall using a pressure sensor mat with a convolutional neural network (CNN) model, and in this study, we aimed to detect the occurrence of falls.

Among various sensing technologies, wearable inertial measurement units (IMUs) have gained significant attention because they are low-cost, privacy-preserving, and easy to deploy. However, two important challenges remain. First, real fall data are extremely limited owing to the safety risks associated with inducing falls in older adults, resulting in a lack of realistic tripping-specific motion patterns. Second, although previous studies have shown that inertial sensors placed near the body's center of gravity provide stable motion information,[6,7] most fall detection studies rely on a single sensor, which restricts the ability to capture multi-segment body dynamics.

To address these issues, we developed a fall-protection system that enables the safe and reproducible collection of fall data. Given the current performance of this protective device, in this study, we conducted controlled experiments only on tripping-induced falls; experiments on slipping and misstep falls are planned for future work after further improvements to the device. Ten subjects performed controlled tripping-fall experiments that included real falls and three types of fall-like daily behavior (FLB) while wearing two IMUs placed on the chest and abdomen. On the basis of the collected data, three long short-term memory (LSTM)-based models were constructed—a chest-sensor model, an abdomen-sensor model, and a dual-sensor model—and evaluated through leave-one-subject-out (LOSO) cross-validation.

The main contributions of this study are summarized as follows:

(1) A safety-assisted fall experiment system was designed to obtain realistic fall data.
(2) A dual torso-mounted IMU configuration was employed to capture upper- and lower-torso dynamics more comprehensively than single-sensor approaches.
(3) Three LSTM-based fall detection models were developed and systematically evaluated under a LOSO scheme, demonstrating that integrating chest and abdominal IMU data significantly improves classification performance.

Taken together, the proposed fall experiment system, dual-torso sensing configuration, and evaluation framework constitute a unified experimental protocol rather than independent methodological elements. The primary contribution of this work lies in the integration of these components to facilitate the systematic investigation of tripping-induced falls, with particular emphasis on distinguishing fall-like behaviors under controlled and safety-assured experimental conditions.

2. Related Works

Recent review articles on sensor-based fall detection systems consistently highlight several unresolved challenges.[8,9] They point out that most existing datasets are collected from young volunteers and contain limited tripping falls, making it difficult for models to generalize to realistic fall scenarios. The reviews also emphasize the difficulty of distinguishing falls from

fall-like daily activities, the limited exploration of multi-sensor configurations, and the lack of standardized evaluation protocols across studies. These limitations indicate the need for more targeted datasets and sensor placements that capture upper-body dynamics relevant to falls.

In addition, a recent comprehensive review by Subramaniam *et al*.[10] systematically summarized inertial- and insole-based wearable sensor systems for fall risk assessment and fall detection, and further noted that, despite the widespread use of IMUs due to their low cost and suitability for long-term monitoring, there is still no clear consensus regarding optimal sensor placement, feature selection, or experimental protocols. The review also observed that many existing studies primarily focus on gait-level spatiotemporal parameters and sensors placed near the lower back or distal body segments, while upper-body kinematics and postural transitions during falls remain comparatively underexplored.

Several recent studies have attempted to address these issues using different sensing modalities and deep learning frameworks. A video-based method combining CNN and LSTM with attention achieved an accuracy higher than 95% accuracy on public RGB video fall datasets,[11] demonstrating the effectiveness of spatiotemporal modeling. However, camera-based systems face privacy constraints and are limited by occlusion and lighting conditions, reducing their suitability for elderly care environments.

A recent sensor-based fall detection study proposed a hybrid temporal convolutional network–gated recurrent unit model that learns spatiotemporal features directly from raw accelerometer and gyroscope signals and evaluated it on public IMU datasets such as MobiAct and a combined MobiAct–SisFall dataset.[12] The model achieved an accuracy of approximately 98–99% in binary fall vs non-fall classification and outperformed several machine learning and deep learning baselines, demonstrating the effectiveness of dilated temporal convolutions combined with gated recurrent units for fall detection. However, in this work, we primarily focused on algorithmic performance on benchmark datasets collected with smartphones and did not systematically investigate how different torso sensor placements or multisensor torso configurations affect upper-body motion representation, leaving open questions about optimal sensor deployment for applications such as posture assessment and protective systems.

A wearable IMU-based hybrid CNN–LSTM model using a single wrist-worn sensor achieved an accuracy of 94–97% on benchmark IMU fall datasets.[13] Wrist sensors can effectively capture abrupt hand motions during a fall, but their ability to reflect torso movement or post-impact posture is limited because the wrist moves largely independently of the body's center of mass. This restricts their usefulness for analyzing upper-body dynamics, which are essential for understanding falls and supporting downstream applications such as posture evaluation and protective system activation.

To address fall-related events prior to ground impact, Wang *et al.* in a recent wearable-sensor-based study investigated near-fall detection during unexpected slip perturbations in over-ground walking among older adults.[14] Using body-worn accelerometer data, they classified loss-of-balance events and reported that an InceptionTime-based model achieved an overall accuracy of approximately 87.5%. While this work demonstrated the feasibility of near-fall detection from wearable sensors, it focused on slip-induced perturbations under laboratory conditions and relied on a single lower-back sensor.

More recently, Schneider *et al*. have further advanced near-fall research by proposing a real-world near-fall detection framework based on the Prev-Fall dataset, which includes slip, trip, and misstep events collected from 110 participants using a dense full-body IMU setup.[15] Their CNN- and InceptionTime-based models achieved weighted F1-scores above 0.85 for near-fall classification. At the same time, the use of 17 IMUs and the occurrence of false positives (FPs) during demanding daily activities highlight limitations in practical wearable deployment.

Building upon these approaches, in this study, we focused specifically on tripping falls and employed inertial sensors placed on the chest and abdomen—locations more strongly coupled with torso motion—to capture upper-body kinematics during and after a fall. By collecting a dedicated tripping dataset and systematically comparing single-sensor and dual-sensor configurations using LSTM-based models, we addressed gaps identified in prior work regarding sensor placement, tripping-specific data collection, and multisensor evaluation. On the other hand, while this study demonstrates the advantages of torso-mounted dual IMUs and a tripping-specific dataset, the proposed method is not intended to replace existing approaches. Instead, it can be integrated with advanced architectures from prior work to achieve higher accuracy and robustness.

3. Materials and Methods

3.1 Behavioral classification

To distinguish tripping falls that occur while walking from other daily behaviors (DBs), human behaviors were first classified on the basis of their association with falls. As shown in Fig. 1, human behaviors were classified into two categories: DBs and fall events (FEs). DBs were further subdivided into two categories: normal DBs (NBs) and FLBs.

The above three behavior types were defined as follows:

FE: This refers to an event in which the person loses balance and falls uncontrollably owing to the restricted movement of the swing leg during gait and inability to shift the center of gravity from the stance leg to the swing leg.

NB: This refers to movements that do not involve significant changes in acceleration or angular velocity during the action. In this study, walking and upright standing are particularly targeted.

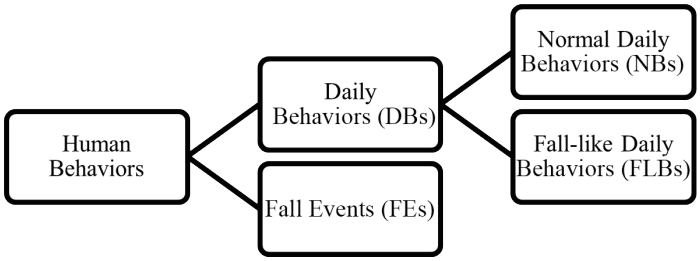

Fig. 1. Behavioral classification.

FLB: This refers to movements that involve large changes in angular velocity or acceleration in a specific direction during the action and that have similarities to falling over. Specifically, these include sitting, lying down, squatting, and bending forward. Running and jumping also involve significant changes in acceleration and angular velocity, but since these actions rarely occur in nursing homes, they are not included in this study, since the elderly and the cared-for are the subjects.[16] In addition, according to existing research,[17] the tendency to change body posture when squatting is almost identical to that of sitting. Therefore, three types of behavior were selected as FLBs in this study: sitting, lying down, and bending forward to pick up objects.

3.2 IMUs

In this study, two TSND151 sensors (Fig. 2, manufactured by ATR-Promotions) were used for data collection. These sensors incorporate the InvenSense MPU-9250 sensor, an acceleration and angular rate sensor. Table 1 shows the specifications of a TSND151 sensor. In addition to accurately recording acceleration and angular velocity data, the TSND151 allows connection to external sensors such as electroencephalography (EEG) electrodes, making it possible to collect multimodal data simultaneously. This capability enables future extensions of the model and integration with additional physiological signals. Moreover, the sensor is compact and lightweight, and supports wireless communication with a computer, minimizing interference with daily activities and ensuring comfort during wear.

To obtain comprehensive motion data, two TSND151 sensors were placed on the subject's chest and abdomen, as illustrated in Fig. 3(a) and shown in Fig. 3(b). Each sensor recorded tri-

Fig. 2. (Color online) TSND151 sensor.

Table 1
TSND151 sensor specifications.[18]

Item	Details
Dimensions	40 mm (W) × 50 mm (H) × 14 mm (D)
Weight	27 g
Communication	Bluetooth Ver. 2.0
Sampling rate	60 Hz

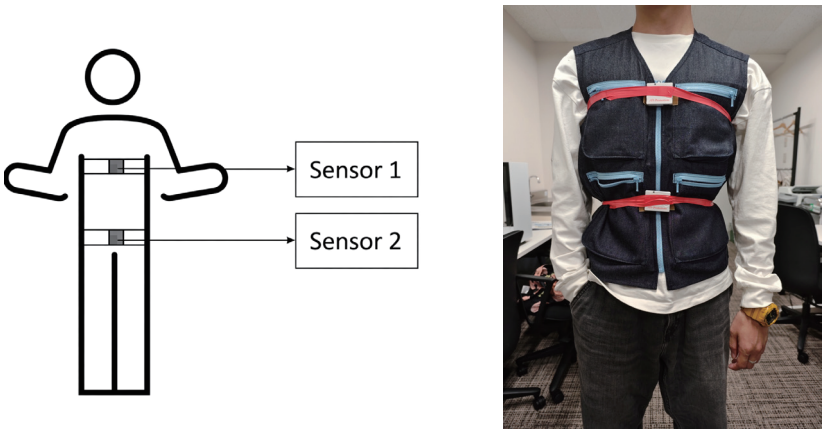

(a) (b)

Fig. 3. (Color online) Placement of sensors on body: (a) schematic illustration of sensor locations and (b) photograph of experimental setup.

axial acceleration and angular velocity, with the *z*-axis oriented in the anterior–posterior direction, the *x*-axis aligned with the vertical direction, and the *y*-axis aligned with the left–right direction. This dual-sensor configuration enabled the collection of kinematic information from different parts of the torso, allowing a more detailed analysis of body movements during a fall.

Existing research[16] has confirmed that the highest accuracy in fall detection is achieved when the IMUs are positioned on the chest and abdomen. These positions are close to the body's center of gravity and provide stable and reliable motion data, which minimizes errors and improves the overall system performance. To enhance accuracy to a greater extent, two sensors were utilized to collect data concurrently. During the training of the model, the data from a single sensor and the data from both sensors were employed for the training and comparison of the results, respectively.

The control software used was ALTIMA, which is a video and sensor data recording and playback software program for multifunctional sensors (for Windows). ALTIMA is a software program that can simultaneously record up to seven small wireless multifunctional sensors (TSND121/151, AMWS020) and up to two channels of video and audio simultaneously.[18] As shown in Fig. 4, the graph on the right-hand side of the operation screen can display in real time the change curves of acceleration and angular velocity in the three axes of the two sensors; the upper left-hand side is the video taken by the camera, and the camera settings are below the video. In this experiment, the video format was set to 1280*720, 60 FPS. Below the video area, there is a button to adjust the video playback speed, with the lowest speed reaching up to 0.01 times the original video speed.

3.3 Fall protection device

To ensure the safety of the subject during the fall experiment, a complete fall protection device was designed and manufactured. As shown in Figs. 5 and 6, the fall protection device consists of a fall protection frame, a protective sponge, and a full harness. The device is 436 cm

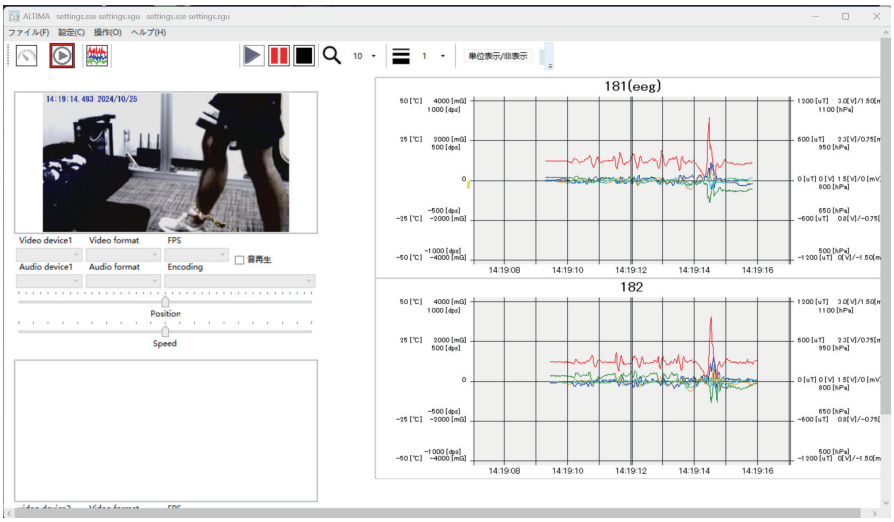

Fig. 4. (Color online) Sample of ALTIMA operating screen.

Fig. 5. (Color online) Configuration of fall protection device.

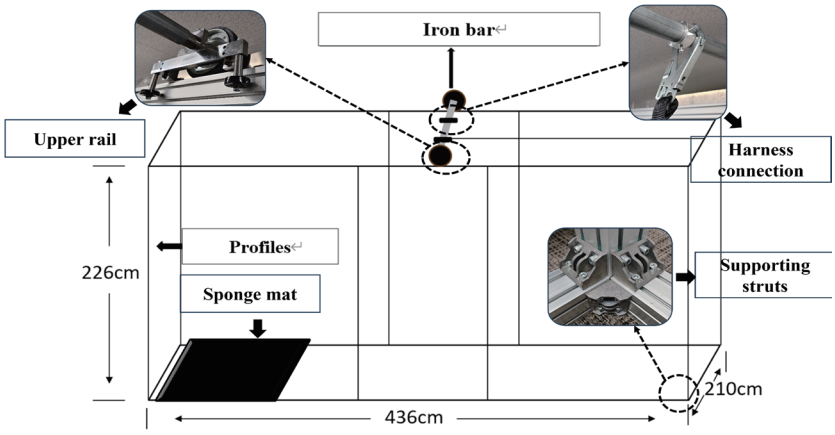

Fig. 6. (Color online) Design diagram for fall protection device.

long, 210 cm wide, and 226 cm high, and weighs approximately 210 kg. The main body of the fall protection frame consists of 20 2.1 m strut profiles with 10 mm slots (manufactured by REXROTH).

The experimenter performed the fall experiment underneath the device while wearing a full harness. An iron bar located above the device and attached to the harness moved with the experimenter, and when a fall occurred, the harness lifted and supported the experimenter from above, while a large sponge beneath the device cushioned the body to prevent contact with the ground.

3.4 Data processing

3.4.1 Dataset

In our experiments, a total of 100 FE trials and 100 trials for each of the three FLB activities were collected using two IMU sensors. On the basis of these data, three models were developed: a model using only chest sensor data, a model using only abdominal sensor data, and a model using data from both sensors.

For the FE trials, the frame corresponding to the peak value of the acceleration magnitude in each trial was first identified. Around this frame, a sliding window of 1.0 s was applied. Starting from the window centered at the peak frame, the window center was shifted in steps of 0.1 s toward both the preceding and subsequent directions, and five additional windows were extracted on each side. Consequently, 11 highly overlapping windows were obtained from each FE trial, resulting in a total of 1100 FE windows.

For the FLB trials, non-overlapping windows with a duration of 1.0 s were extracted sequentially from the beginning of each trial, without applying any overlap. This procedure yielded 4424 FLB windows.

To prevent data leakage, dataset partitioning was performed at the subject level. The 10 subjects were divided into training, validation, and test sets with a ratio of 8:1:1 using a LOSO scheme, in which, for each fold, the data from eight subjects were used for training, one subject for validation, and one subject for testing. For the test data, the entire sequence of each trial was segmented using a sliding window with a length of 1.0 s and a step size of 0.1 s.

3.4.2 Filters

To mitigate sensor noise, the raw acceleration data were first processed with a median filter to remove sudden spikes caused by sensor disturbances. Then, a third-order low-pass Butterworth filter with a cutoff frequency of 20 Hz was applied. The Butterworth filter was chosen for its smooth frequency response, and the 20 Hz cutoff was selected because most human motion signals fall within the 0–15 Hz range; a slightly higher threshold ensures the full capture of relevant motion while filtering out high-frequency noise.

Additionally, since the acceleration data includes both body movement and gravity, another low-pass Butterworth filter with a cutoff frequency of 0.3 Hz was used to estimate the gravitational component. This is because gravity changes slowly compared with human motion. By subtracting this low-frequency component, the dynamic acceleration of the human body can be more accurately isolated. This filtering approach has been validated in related studies and has proven effective in both noise reduction and acceleration separation.[19]

3.4.3 Feature extraction

After filtering the data, we chose the following instantaneous features along with the raw three-axis acceleration and angular velocity values as inputs to the model.

As shown in Table 2, the acceleration magnitude indicates the magnitude of the synthetic acceleration on the three axes, which reflects the change in the experimenter's movement intensity; the angular velocity magnitude indicates the magnitude of the synthetic angular velocity, which reflects the change in the experimenter's posture. Jerk is used to detect sudden changes in acceleration, and a pronounced jerk usually occurs during a fall. For training the model using data from a single sensor, the raw data from the corresponding sensor and the above three data computed on the basis of the raw data are used as features. For models trained using data from two sensors, the acceleration and angular velocity angles between the two sensors are included in addition to the above features.

Here, a_x, a_y, and a_z are the acceleration components along the *x*-, *y*-, and *z*-axes, and ω_x, ω_y, and ω_z are the angular velocity components along the *x*-, *y*-, and *z*-axes, respectively. Moreover, $\vec{a}$ is the acceleration vector, $\vec{\omega}$ is the angular velocity vector, and $|\vec{a}|$ and $|\vec{\omega}|$ are the magnitudes of the acceleration and angular velocity vectors, respectively. *Jerk* is the rate of change of the acceleration magnitude, Δt is the time interval between two consecutive samples, θ is the angle between two acceleration vectors, θ_ω is the angle between two angular velocity vectors, and $\overrightarrow{a_1}$ and $\overrightarrow{a_2}$ are the acceleration vectors from sensors 1 and 2, and $\overrightarrow{\omega_1}$ and $\overrightarrow{\omega_2}$ are the angular velocity vectors from sensors 1 and 2, respectively.

Table 2
Features of input model and their calculation formulae.

Feature	Formula
Acceleration magnitude	$\lvert\vec{a}\rvert = \sqrt{a_x^2 + a_y^2 + a_z^2}$
Angular velocity magnitude	$\lvert\vec{\omega}\rvert = \sqrt{\omega_x^2 + \omega_y^2 + \omega_z^2}$
Jerk	$Jerk = \frac{d\lvert\vec{a}\rvert}{dt} \approx \frac{\lvert\vec{a}(t)\rvert - \lvert\vec{a}(t-1)\rvert}{\Delta t}$
Angle between two sensors (acceleration)	$\theta = \arccos\left(\frac{\overrightarrow{a_1} \cdot \overrightarrow{a_2}}{\lvert\overrightarrow{a_1}\rvert \cdot \lvert\overrightarrow{a_2}\rvert}\right)$
Angle between two sensors (acceleration velocity)	$\theta_\omega = \arccos\left(\frac{\overrightarrow{\omega_1} \cdot \overrightarrow{\omega_2}}{\lvert\overrightarrow{\omega_1}\rvert \cdot \lvert\overrightarrow{\omega_2}\rvert}\right)$

3.4.4 *Z*-score normalization

To facilitate the faster convergence of the LSTM model and prevent any single feature from dominating the learning process owing to its larger numerical scale, the raw sensor data and derived feature values were standardized using the *Z*-score normalization method. The standardization formula is expressed as

$$z = \frac{x - \mu}{\sigma}, \tag{1}$$

where x is the original feature value, μ is the mean of the feature, and σ is the standard deviation of the feature.

This transformation ensures that each feature has a mean of 0 and a standard deviation of 1, thereby improving numerical stability and accelerating gradient-based optimization in the LSTM training process.

3.4.5 LSTM

LSTM is a deep learning model specializing in the analysis of time-series data and is a type of recurrent neural network (RNN) that can consider long-term dependencies.[20] RNN is a powerful method for processing time-series data, but its performance is often limited in tasks that require long-term dependencies. Designed as an improved version of RNN, LSTM features cell states and three gates (forget gate, input gate, and output gate), as shown in Fig. 7. The input at each time step is denoted as x_t, and the hidden state as h_t, which carries information forward through the sequence. The LSTM cell (A) maintains a state, which is passed along the time axis and updated through the three gates. The forget gate decides which information from the previous cell state should be discarded, the input gate determines which new information to add, and the output gate decides how much of the cell state should be exposed as the hidden state. The sigmoid function (σ) outputs values between 0 and 1, acting as a filter in the gates, whereas the tanh function scales data between –1 and 1 to regulate the signal. ⊗ represents element-wise

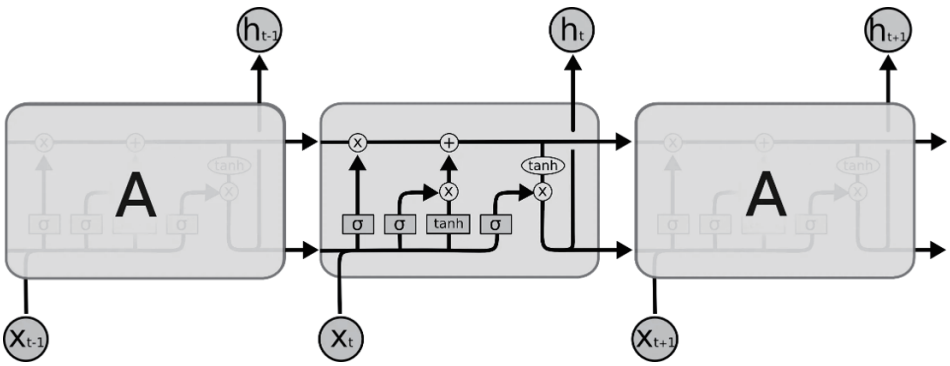

Fig. 7. Composition of LSTM cell.[21]

multiplication, typically used to gate information (e.g., controlling what portion of the cell state is retained or passed on), whereas ⊕ denotes element-wise addition, used to update the cell state by combining the retained old state and the new candidate values. Arrows in the figure indicate the flow of data between components and across time steps.

Owing to these structures, LSTM can retain, update, and discard information dynamically. In this study, the LSTM model was used to analyze time series changes in behavior from acceleration and angular velocity data, and to detect falls. The input data are time-series data of acceleration and angular velocity obtained from sensors, which are input to the model in the form of learning changes along the time series. The output of the LSTM model represents the identification results of the behavior based on the time-series data, aiming to improve the accuracy of fall detection.

The LSTM structure used in this study is shown in Fig. 8. The temporal length of input data is 60 (60 Hz × 1 s), and the batch size for a single input is set to 16. A smaller batch size helps mitigate local-optima issues in small-sample scenarios by introducing greater stochasticity into gradient updates.

For feature dimensions (D), the single-sensor model uses 9 features (6 triaxial raw data + 3 artificial features), while the dual-sensor model uses 20 features (12 triaxial raw data from two sensors + 8 artificial features). Owing to the limited sample size, the model adopts a single-layer LSTM structure with 32 hidden units and a dropout rate of 0.1 to mitigate overfitting. The Adam optimizer (with a default learning rate of 0.001) is selected for training, and the model is trained for 30 epochs.

After the LSTM layer, the model connects a dense layer that takes the final hidden state of the sequence as output. This dense layer maps the 32-dimensional hidden state from LSTM to 16 dimensions, introducing nonlinearity through Rectified Linear Unit (ReLU) activation. The ReLU activation function is one of the most used activation functions in deep learning. It is defined as

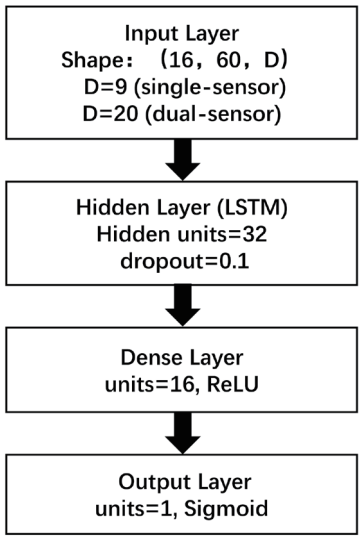

Fig. 8. LSTM structure used in this study.

$$ReLU(x) = \max(0, x). \tag{2}$$

This function introduces nonlinearity by returning the input value when it is positive and zero otherwise. Compared with traditional activation functions such as sigmoid and tanh, ReLU helps mitigate the vanishing gradient problem, speeds up convergence, and improves training efficiency, especially in deep networks.

The output layer uses sigmoid activation to map results to the [0,1] interval for binary classification probabilities, and employs BinaryCrossentropy as the loss function for model optimization. Commonly used activation functions include sigmoid, tanh, ReLU, and SoftMax. Among them, sigmoid is defined as

$$\sigma(x) = \frac{1}{1 + e^{-x}}. \tag{3}$$

The sigmoid function maps input values to the range [0, 1], making it suitable for binary classification tasks in which the output represents a probability. In this study, the sigmoid function was used in the final output layer to provide a probabilistic prediction of whether a fall occurred. Other activation functions, such as SoftMax and tanh, are more appropriate for multi-class classification and recurrent structures, respectively, with tanh providing a symmetric output range of [−1, 1].

4. Experiments

4.1 Experimental setting

The experimental equipment included two TSND151 sensors, a personal computer with ALTIMA software installed, a fall protection device, a USB camera (ELP-USBFHD08s-MFV, 5–50 mm) with a tripod mount, a chair, a bed, a tape measure used as a target for the pick-up movement, gummed tape for fixing the sensors, a rope for restricting the swing leg, and a rigid sleeveless jacket.

The experiments were conducted in the Tajima Laboratory, located on the 8th floor of Building B at Fukuoka Institute of Technology. The experimental environment consisted of a flat floor covered with a relatively hard carpet.

The subjects were ten students from Fukuoka Institute of Technology, aged 20–24 years, with heights ranging from 170 to 182 cm and body weights ranging from 55 to 71 kg.

4.2 Experimental preparation

The subject wears a rigid sleeveless jacket, and the chest sensor is attached. The sensor is adjusted so that its upper edge is at the same height as the armpit, and experimental duct tape is wrapped around the body to fix the sensor in place. The sleeveless jacket serves to prevent the

sensors from being improperly inclined due to wrinkles in the clothing and from being biased out of alignment with the subject's torso. The abdominal sensor is then attached and adjusted so that the top of the sensor is at the same height as the navel. The rest of the fixing procedure is the same as for the chest sensor.

4.3 Fall-like behavior experiments

4.3.1 Sitting experiment

A chair is placed in front of the camera, and the subject is asked to start walking from a fixed position. After walking to the chair, the subject sits on the chair, waits for a moment, and then stands up and returns to the starting position. Each subject performs this 10 times.

4.3.2 Lying down experiment

A bed is placed in front of the camera, and the subject is asked to start walking from a fixed position. After walking to the bed, the subject lies down on the bed, waits for a while, and then stands up and returns to the starting position. Each subject performs this 10 times.

4.3.3 Forward bending experiment

A tape measure that can be picked up with one hand is placed on the floor in front of the camera to be picked up by bending forward, and the subject is asked to start walking from a fixed position. After walking to the tape measure, the subject picks it up, stands upright, and waits for a few moments before placing the tape measure in its original position and returning to the starting position. The subject is instructed to pick up the object using a forward bending posture rather than a crouching posture. Each subject performs this 10 times.

4.4 Falling experiment

Subjects were fitted with full harness prior to the experiment. As each subject had a different body shape, the harness was carefully adjusted and confirmed to be securely fastened to ensure safety throughout the experiment. At the beginning of each trial, the subject stood at the walking starting position with the heel of the rear foot placed in contact with the frame, defining a consistent initial walking posture, as illustrated in Fig. 9.

Before formal data collection, the subject was asked to attempt several practice falls in front of the protective sponge while wearing the harness. No data was recorded during this familiarization stage. After the subject confirmed readiness, a rope padded with foam was attached to one ankle, while the opposite leg was instructed to initiate the walking motion. The subject was asked to walk with a natural stride length. The position corresponding to the fifth step was identified, and the protective sponge and cameras were repositioned so that the subject would land on the sponge in the event of a fall.

After these preparations, the fall experiment was formally initiated. The subject walked with the same stride length as during the practice trials. After the fifth step and while the sixth step was in progress, the rope was pulled to restrict the motion of the ankle and disturb the center of gravity, thereby inducing a forward fall. Figure 10 illustrates the ankle rope configuration, and Fig. 9 provides a schematic overview of the walking starting position, approximate tripping location, and experimental layout. A camera was placed outside the protective apparatus, and the shaded region in Fig. 9 represents the approximate camera field of view used for recording the fall motion. Each subject performed ten fall trials, consisting of five falls induced by the left foot and five induced by the right foot. To prevent anticipatory behavior and unnatural motion patterns, additional walking trials without falls were conducted, during which FEs were randomly introduced without prior notification.

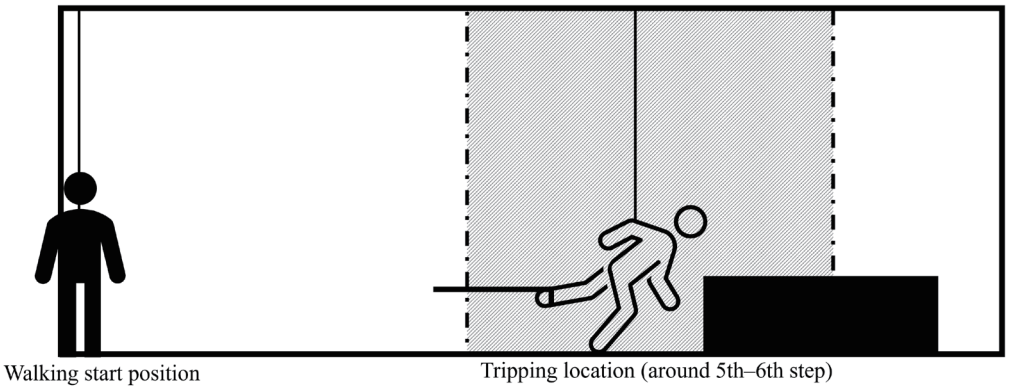

Fig. 9. Diagram of fall experiment.

Fig. 10. (Color online) Rope attached to leg.

Ethical approval for this study was obtained from the Human Research Ethics Committee of Fukuoka Institute of Technology (approval ID: hm02-25, approved on 9 May 2025). All participants were fully informed of the experimental procedures, potential risks, and data handling policies prior to participation, and written informed consent was obtained from all subjects. Participation was voluntary, and participants were free to withdraw from the experiment at any time without penalty. To ensure participant safety during induced fall experiments, a full-body safety harness and sponge mats were used, and all experiments were conducted under the safety guidelines approved by the ethics committee. Experiments were immediately terminated if any safety concerns arose.

5. Results

A LOSO cross-validation procedure was employed to rigorously assess the subject-independent performance of the proposed models. In each fold, the data from one subject were assigned exclusively to the test set, whereas the data from the remaining subjects were used for model training and validation. This procedure ensured that every subject served as the test subject once, thereby eliminating subject-specific bias and enabling a comprehensive evaluation across all individuals.

Tables 3–5 present the confusion matrices obtained from the chest sensor model, the abdomen sensor model, and the dual-sensor model, respectively, and Table 6 summarizes their overall accuracy, precision, recall, and F1-score. To further examine the variability of model performance across subjects under the LOSO scheme, Fig. 11 presents boxplots of per-subject accuracy, precision, recall, and F1-score for the dual-sensor model. In these boxplots, the boxes represent the interquartile range from the first to the third quartile across subjects, and the

Table 3
Confusion matrices of chest sensor model.

Chest Sensor Model	Predicted FE	Predicted FLB
Actual FE	95	4
Actual FLB	12	288

Table 4
Confusion matrices of abdomen sensor model.

Abdomen Sensor Model	Predicted FE	Predicted FLB
Actual FE	91	9
Actual FLB	15	285

Table 5
Confusion matrices of dual-sensor model.

Dual-sensor Model	Predicted FE	Predicted FLB
Actual FE	98	2
Actual FLB	7	293

Table 6
Accuracy, precision, recall, and F1-score of three models.

Model type	Accuracy (%)	Precision (%)	Recall (%)	F1-score (%)
Chest sensor model	95.99	88.79	95.96	92.25
Abdomen sensor model	94.00	85.85	91.00	88.40
Dual-sensor model	97.75	93.33	98.00	95.61

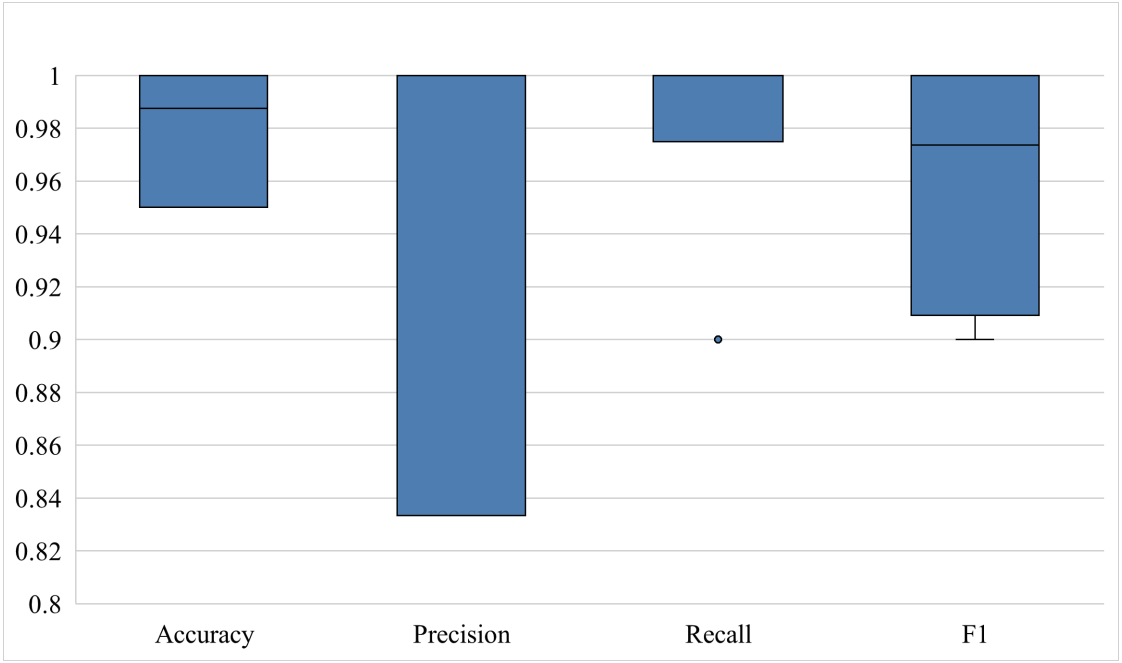

Fig. 11. Per-subject performance distributions under LOSO scheme for dual-sensor model.

central lines indicate the medians. The whiskers denote the minimum and maximum values of each metric, illustrating the inter-subject variability of model performance under the LOSO scheme. For visualization purposes, all metrics are shown on a normalized scale ranging from 0 to 1, whereas Table 6 shows the corresponding values in percentage form. The results indicate consistently high recall across subjects with limited inter-subject variation. Across all LOSO folds, the dual-sensor model achieved a mean recall of 98.00%, with a 95% confidence interval of [94.98%, 100.00%], demonstrating stable subject-independent fall detection performance. In contrast, precision exhibited larger inter-subject variability, reflecting differences in false-positive occurrences among fall-like activities. Among the three models, the dual-sensor configuration demonstrated the highest performance, achieving an accuracy of 97.75%, a precision of 93.33%, a recall of 98.00%, and an F1-score of 95.61%. The chest sensor model also exhibited strong performance (accuracy: 95.99%, precision: 88.79%, recall: 95.96%, and F1-score: 92.25%), followed by the abdomen sensor model (accuracy: 94.00%, precision: 85.85%, recall: 91.00%, and F1-score: 88.40%).

To mitigate the risk of missed detections, a comparatively low decision threshold was adopted for the sigmoid output layer. Lowering the threshold increased the likelihood of classifying

borderline cases as falls, thereby improving sensitivity. To identify an optimal value, threshold candidates ranging from 0.10 to 0.50 were evaluated in increments of 0.01. The most favorable trade-off between sensitivity and specificity was obtained at a threshold of 0.41. To avoid potential data leakage, the decision threshold was selected exclusively using the training and validation data within each LOSO fold. Specifically, for each fold, the model was trained on data from $N-1$ subjects, and the threshold was determined solely on the basis of the corresponding validation results without any access to the held-out test subject. The finalized threshold and window-based decision rule were then applied to the test subject in that fold without further adjustment.

Furthermore, a sequential decision mechanism was incorporated to enhance detection robustness. A trial was classified as a fall only when nine consecutive sliding windows were predicted as falls. This approach, which had been validated in prior studies,[12] also proved effective in the present work by suppressing isolated false-positive predictions while reliably capturing true FEs.

Table 7 shows the distribution of false negatives (FNs) and FPs of the dual-sensor model by activity type. Two FNs were observed during FEs. Among the FPs, one occurred during a sitting motion and six occurred during forward-bending activities, while no FPs were observed during lying-down motions. These results indicate that dynamic activities involving substantial forward torso flexion were more likely to be misclassified as falls under the adopted low-threshold setting.

6. Discussion

The comparison of the single-sensor models indicated that the chest sensor model outperformed the abdomen sensor model in all evaluation metrics. This difference was considered consistent with the biomechanical characteristics of tripping-induced falls. During loss of balance, the upper torso typically underwent larger and more rapid forward and downward rotations, producing more distinctive acceleration and angular velocity patterns at the chest. In contrast, the abdomen, located closer to the body's center of mass, exhibited relatively smoother and damped kinematic variations, thereby reducing its discriminative ability. Consequently, fall-related features were more salient in the chest-mounted IMU data than in the abdominal IMU data.

The dual-sensor model demonstrated superior performance compared with both single-sensor models. By integrating complementary kinematic information from the chest and abdomen, the model captured a more complete representation of torso dynamics during fall

Table 7
Distribution of FNs and FPs of dual-sensor model by activity type.

Activity type	FN	FP
Fall (FE)	2	—
Sitting (FLB)	—	1
Lying down (FLB)	—	0
Forward bending (FLB)	—	6

initiation. The combination of upper- and lower-torso motion patterns effectively reduced ambiguity in fall-like activities and contributed to significant improvements in accuracy, precision, recall, and F1-score. These results highlighted the advantage of multi-point sensing in detecting tripping-induced falls.

Note that all experimental data in this study were collected from young adults. This choice was primarily motivated by safety and ethical considerations, as inducing falls in elderly individuals entails substantial risk. As a result, the movement characteristics and fall dynamics observed in this study may not fully represent those of older or physically frail populations. This limitation should be considered when interpreting the applicability of the proposed method to real-world elderly care scenarios.

The FNs may have occurred because some subjects subconsciously attenuated their fall motions. Although the experimental procedure was designed to introduce falls randomly and reduce anticipatory behavior, subjects might still have maintained a high degree of vigilance during repeated trials. As a result, certain falls were performed in a more controlled manner, generating relatively weak kinematic signatures that resembled non-fall behaviors. Future studies may consider further increasing the unpredictability of fall occurrence (for example, by obstructing subjects' vision or introducing more complex concurrent tasks) to divert attention and reduce their ability to continuously anticipate upcoming falls.

Most FPs occurred during sitting and forward-bending movements. These activities involved large-amplitude torso flexion and produced characteristic peaks in the x-axis and z-axis acceleration as well as notable changes in y-axis angular velocity. Combined with the intentionally low sigmoid threshold adopted to minimize missed detections, these high-magnitude signals were more likely to be classified as falls. This observation suggested that certain dynamic daily activities with substantial torso flexion may require additional modeling strategies. One possible direction is the incorporation of other physiological signals (such as EEG) to estimate the subject's emotional or cognitive state, which may help distinguish between genuine falls and non-fall behaviors that merely exhibit large motion dynamics, thereby further reducing false alarms.

7. Conclusions and Future Work

In this study, a fall detection method utilizing dual IMUs and an LSTM network was proposed and evaluated through a series of controlled tripping-induced fall experiments. A fall-protection apparatus was constructed to ensure that real fall data can be collected safely and repeatedly. During the experiments, IMU sensors were placed on the chest and abdomen of each subject, and both FEs and three types of fall-like behavior were recorded. On the basis of these data, three models were developed: a chest-sensor model, an abdomen-sensor model, and a dual-sensor model integrating both data sources.

A LOSO cross-validation scheme was employed to assess subject-independent performance. For the fall-event data, heavily overlapped 1 s windows centered around the peak acceleration frame were extracted, whereas non-overlapping windows were used for fall-like behaviors. For the test data, sliding windows with a length of 1.0 s and a step of 0.1 s were applied across the

entire sequence, enabling fine-grained temporal evaluation. To reduce missed detections, a relatively low sigmoid threshold was adopted and optimized, with the best performance obtained at a threshold of 0.41. Furthermore, a sequential decision rule was used, in which a trial was classified as a fall only when nine consecutive windows were predicted as falls.

Experimental results demonstrated that the dual-sensor model achieved the highest accuracy, precision, recall, and F1-score among the three configurations, confirming the advantage of combining complementary kinematic information from both the upper and lower torso. The results also indicated that sensor placement had a substantial effect on performance, with the chest sensor outperforming the abdomen sensor. These findings verified the effectiveness of the proposed method in improving the robustness of tripping-induced fall detection.

As for future work, several directions will be pursued to extend the applicability of the proposed method to more representative target populations. First, the dataset will be expanded with additional subjects and more diverse fall scenarios to further improve model generalization. To better reflect fall dynamics in older or physically frail populations, future studies will also explore the use of aging-simulation equipment and biomechanical constraints to model age-related changes in mobility, balance, and reaction characteristics under safe experimental conditions. In addition, the effect of safety devices will be further examined by optimizing harness configuration, such as tuning harness slack and attachment conditions, to minimize interference with natural fall kinematics.

Second, more advanced deep learning architectures, including attention-based models, temporal convolutional networks, and hybrid fusion frameworks, will be investigated to enhance detection performance. Third, strategies to reduce FPs will be explored, including the incorporation of additional physiological signals such as EEG to assess the subject's emotional or cognitive state and thereby distinguish genuine falls from vigorous non-fall activities. Finally, beyond fall detection, future research will focus on fall prediction. The long-term goal is to integrate the proposed method into a wearable safety airbag system capable of predicting falls in advance and localizing potential injury regions to enable the targeted deployment of protective devices.

References

1 Tokyo Fire Department: Elderly Accidents Seen from Emergency Transport Data. http://www.tfd.metro.tokyo.lg.jp/ (accessed October 2025).
2 Cabinet Office, Government of Japan: Annual Report on the Aging Society: 2023 Edition. http://www8.cao.go.jp/kourei/whitepaper/index.html (accessed October 2025).
3 K. Fujita, Y. Fujiwara, S. Kumagai, S. Watanabe, Y. Yoshida, Y. Motohashi, and S. Shinkai: Nihon Koshu Eisei Zasshi **51** (2004) 168.
4 J. Zhang, T. Tajima, and T. Abe: J. Jpn. Soc. Welfare Eng. **25** (2023) 29.
5 J. Zhang and T. Tajima: J. Comput. Commun. **8** (2020) 73. https://doi.org/10.4236/jcc.2020.812007
6 M. Gjoreski, H. Gjoreski, M. Luštrek, and M. Gams: Sensors **16** (2016) 800. https://doi.org/10.3390/s16060800
7 M. H. Rahmani, R. Berkvens, and M. Weyn: Chest-Worn Inertial Sensors: Sensors **21** (2021) 2875. https://doi.org/10.3390/s21082875
8 S. Nooruddin, M. M. Islam, F. A. Sharna, H. Alhetari, and M. N. Kabir: J. Ambient Intell. Humaniz. Comput. **13** (2022) 2735. https://doi.org/10.1007/s12652-021-03248-z
9 S. Usmani, A. Saboor, M. Haris, M. A. Khan, and H. Park: Sensors **21** (2021) 5134. https://doi.org/10.3390/s21155134

10 S. Subramaniam, A. I. Faisal, and M. J. Deen: Front. Digit. Health **4** (2022) 921506. https://doi.org/10.3389/fdgth.2022.921506
11 Q. Feng, C. Gao, L. Wang, Y. Zhao, T. Song, and Q. Li: Pattern Recognit. Lett. **130** (2020) 242. https://doi.org/10.1016/j.patrec.2018.08.031
12 Y. Li, Z. Zuo, and J. Pan: Future Gener. Comput. Syst. **139** (2023) 53. https://doi.org/10.1016/j.future.2022.09.011
13 X. Hu, S. Yu, J. Zheng, Z. Fang, Z. Zhao, and X. Qu: Adv. Eng. Inform. **65** (2025) 103178. https://doi.org/10.1016/j.aei.2025.103178
14 S. Wang, F. Miranda, Y. Wang, R. R. E. Romijnders, J. B. J. Bussmann, and J. H. van Dieën: Sensors **22** (2022) 3334. https://doi.org/10.3390/s22093334
15 M. Schneider, K. Seeser-Reich, A. Fiedler, L. Becker, and B. M. Eskofier: Sensors **25** (2025) 1468. https://doi.org/10.3390/s25051468
16 H. Gjoreski, M. Luštrek, and M. Gams: Proc. 2011 7th Int. Conf. Intelligent Environments (IEEE, 2011) 47–54. https://doi.org/10.1109/IE.2011.11
17 D. Niu, Y. Liu, T. Cai, C. Peng, Y. Zhan, and J. Liang: CAAI Trans. Intell. Syst. **13** (2018) 380. https://doi.org/10.11992/tis.201710013
18 ATR-Promotions Inc.: TSND151 Users' Manual. https://www.atr-p.com/products/pdf/TSND151-usersmanual.pdf (accessed October 2025).
19 S. Fan, Y. Jia, and C. Jia: Information **10** (2019) 290. https://doi.org/10.3390/info10100290
20 A. Graves: Long Short-Term Memory, in Supervised Sequence Labelling with Recurrent Neural Networks (Springer, Berlin, 2012).
21 R. C. Staudemeyer and E. R. Morris: arXiv:1909.09586 (2019). https://arxiv.org/abs/1909.09586